

Computational Fluid Dynamics: Final Project Report

Shantanu Bailoor

*The Johns Hopkins University
Baltimore, MD, USA 21218*

Abstract

The development of a two-dimensional, viscous, incompressible Navier-Stokes solver is described in this report. The second-order central difference scheme is used for discretizing derivatives and Chorin's fractional-time method is used for time-advancement. The advective fluxes are integrated explicitly using a second-order Adams-Bashforth scheme while the diffusive fluxes are computed implicitly with the second-order Crank-Nicolson scheme. Pointwise Gauss-Seidel and SOR based linear solvers are implemented to iteratively invert the implicit momentum and the pressure Poisosn systems, respectively. Fluid-solid interaction is modeled using a first-order ghost-cell based immersed boundary method. Results are presented for flow past a square cylinder in a rectangular channel at Re 50 and 150 and compared with published results. Grid and domain dependence studies are performed on with Re 150. Good agreement is established in each case with data available in literature. Finally, flow past a circular cylinder with 20% blockage, confined in a channel at Re 100 is simulated and results compared with established data. In each case, flow features in the wake and Strouhal number are compared and found to be in excellent agreement with those reported in the respective papers.

Keywords: Computational Fluid Dynamics, Immersed Boundary Method, Strouhal Number, Finite-Difference Method.

Email address: shantanub@jhu.edu (Shantanu Bailoor)

1. Introduction and Objectives

This report describes the development of a numerical two-dimensional viscous, incompressible Navier-Stokes equation solver. Flow around bluff bodies have been widely tested for several decades and are therefore great candidates for benchmarking and validation. The objectives for this study are thus outlined:

1. Discretize the Navier-Stokes equations on a rectangular domain using a Cartesian mesh.
2. Implement appropriate spatial discretization and time-advancement schemes for the various fluxes that appear in the Navier-Stokes equations.
3. Incorporate suitable Cartesian grid method to simulate the interaction between fluid and an immersed rigid body.
4. Test whether the solver can accurately simulate Poiseuille flow in a channel in the absence of any obstruction.
5. Simulate flow over square/ circular cylinder and comment on the flow features around the immersed body.
6. Compare obtained results with published data in the literature, based on flow parameters and non-dimensional numbers of the flow.

2. Methods

2.1. Discretization of the Navier-Stokes equations

The two-dimensional, incompressible Navier Stokes equations can be written in the non-dimensionalized conservation form as:

$$\frac{\partial u_i}{\partial x_i} = 0 \quad (1)$$

$$\frac{\partial u_i}{\partial t} + \frac{\partial}{\partial x_j} (u_i u_j) = - \frac{\partial p}{\partial x_i} + \frac{1}{Re} \frac{\partial}{\partial x_j} \left(\frac{\partial}{\partial x_j} (u_i) \right) \quad (2)$$

Equations 1 and 2 are discretized on a grid such as one shown in Figure 1, where the variables (u, v, p) are collocated at the cell-centers. Additional face-center velocities are defined for computing the convective fluxes and the source terms for the pressure Poisson equation and will be discussed in greater detail later.

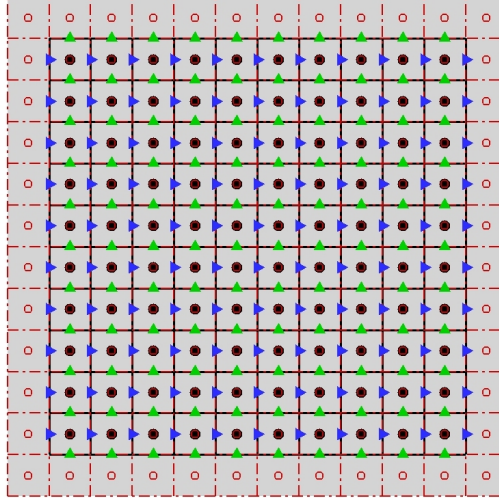


Figure 1: Grid layout indicating locations of cell-center fluid variables (●), ghost-cell fluid variables (○) x - (▷) and y - (△) velocity components on face centers.

The convective fluxes are discretized using both, the cell-centered and face-centered velocities. In principle, the cell-centered velocity, also the velocity being marched in time in the momentum equation, can be perceived to be convected by the face-centered velocity components, in and out of each finite cell. Thus, if (u, v) and (U, V) are the cell-centered and face-centered velocities, respectively, the convective flux at cell (I, J) can be evaluated as:

$$\frac{\partial}{\partial x_j} (u_i U_j)_{i=1} = \frac{(uU)_e - (uU)_w}{\Delta x} + \frac{(uV)_n - (uV)_s}{\Delta y} \quad (3)$$

$$\frac{\partial}{\partial x_j} (u_i U_j)_{i=2} = \frac{(vU)_e - (vU)_w}{\Delta x} + \frac{(vV)_n - (vV)_s}{\Delta y} \quad (4)$$

In the above equations, the subscripts e, w, n, s indicate that the quantities are evaluated at the east, west, north and south face-centers of the cell, respectively. Δx and Δy are the grid spacings along x - and y -, respectively. The uppercase, face-center velocities are readily available at the required locations, the cell-centered velocities are interpolated between adjacent cell-centers, for example, over a uniformly spaced grid:

$$u_e = \frac{u_P + u_E}{2} = \frac{u_{I,J} + u_{I+1,J}}{2} \quad (5)$$

The diffusive fluxes are evaluated as:

$$\begin{aligned} \frac{1}{Re} \frac{\partial^2}{\partial x_j^2} (u_i)_{i=1} &= \frac{1}{Re} \left[\frac{1}{\Delta x} \left(\frac{\partial u}{\partial x}|_e - \frac{\partial u}{\partial x}|_w \right) + \frac{1}{\Delta y} \left(\frac{\partial u}{\partial y}|_n - \frac{\partial u}{\partial y}|_s \right) \right] \\ &= \frac{1}{Re} \left(\frac{u_{I+1,J} - 2u_{I,J} + u_{I-1,J}}{\Delta x^2} + \frac{u_{I,J+1} - 2u_{I,J} + u_{I,J-1}}{\Delta y^2} \right) \end{aligned} \quad (6)$$

Likewise, the diffusive fluxes for the y -momentum equation can be derived as:

$$\frac{1}{Re} \frac{\partial^2}{\partial x_j^2} (u_i)_{i=2} = \frac{1}{Re} \left(\frac{v_{I+1,J} - 2v_{I,J} + v_{I-1,J}}{\Delta x^2} + \frac{v_{I,J+1} - 2v_{I,J} + v_{I,J-1}}{\Delta y^2} \right) \quad (7)$$

Further, the convective fluxes are integrated using the single-stage, second-order Adams Bashforth scheme and the diffusive fluxes integrated using the implicit Crank-Nicolson scheme. Thus, the semi-discrete momentum equation, excluding pressure fluxes can be written as:

$$\frac{u^* - u^n}{\Delta t} = -\frac{3}{2} \frac{\partial}{\partial x_j} (u_i U_j)^n + \frac{1}{2} \frac{\partial}{\partial x_j} (u_i U_j)^{n-1} + \frac{1}{2Re} \frac{\partial^2}{\partial x_j^2} (u^* + u^n) \quad (8)$$

The Adams-Bashforth scheme requires information at current and one previous time-step. Thus, it is not self-starting. The first time-step is advanced using first-order forward Euler scheme.

At the *right boundary*, the east face is part of the outlet boundary condition (zero normal-gradient). This gives rise to the condition: $u_E = u_P; v_E = v_P$. The convective flux can be approximated as:

$$\begin{aligned} NL_1 &= \frac{(u_P U_b) - (u U)_w}{\Delta x} + \frac{(u V)_n - (u V)_s}{\Delta y} \\ NL_2 &= \frac{(v_P U_b) - (v U)_w}{\Delta x} + \frac{(v V)_n - (v V)_s}{\Delta y} \end{aligned} \quad (9)$$

Note that the mass-balance condition is applied to the intermediate velocities and not the time-level velocities. Similarly, the diffusive flux reduces to:

$$L_1 = \frac{1}{Re} \left[\frac{u_W - u_P}{\Delta x^2} + \frac{u_N - 2u_P + u_S}{\Delta y^2} \right] \quad (10)$$

$$L_2 = \frac{1}{Re} \left[\frac{v_W - v_P}{\Delta x^2} + \frac{v_N - 2v_P + v_S}{\Delta y^2} \right]$$

At the *lower left corner*, the west face is subject to the inlet boundary condition and the bottom face is subject to no-slip, no-penetration boundary condition. This implies $V_w = 0; u_w = U_w = U_b = 1 - 4 \left(\frac{2H - \Delta y}{2H} \right)^2$ and $U_s = V_s = 0$. The convective flux NL reduces to:

$$NL_1 = \frac{(uU)_e - U_b^2}{\Delta x} + \frac{(uV)_n}{\Delta y} \quad (11)$$

$$NL_2 = \frac{(vU)_e}{\Delta x} + \frac{(vV)_n}{\Delta y}$$

For the diffusive fluxes, the boundary conditions imply $u_W = 2U_b - u_P$ and $u_P = -u_S; v_P = -v_S$. L can be computed as:

$$L_1 = \frac{1}{Re} \left[\frac{u_E - 3u_P + 2U_b}{\Delta x^2} + \frac{u_N - 3u_P}{\Delta y^2} \right] \quad (12)$$

$$L_2 = \frac{1}{Re} \left[\frac{v_E - 3v_P}{\Delta x^2} + \frac{v_N - 3v_P}{\Delta y^2} \right]$$

2.2. Poisson Solver

The pressure Poisson equation is discretized using the second-order central difference scheme. *In the bulk of the domain*, the discrete pressure Laplacian takes the form:

$$\frac{\partial}{\partial x_j} \frac{\partial}{\partial x_j} p = \frac{p_E - 2p_P + p_W}{\Delta x^2} + \frac{p_N - 2p_P + p_S}{\Delta y^2} \quad (13)$$

At the *right boundary*, we have $\frac{\partial p}{\partial x_e} = 0$, which implies $p_E = p_P$. Therefore:

$$\frac{\partial}{\partial x_j} \frac{\partial}{\partial x_j} p = \frac{-p_P + p_W}{\Delta x^2} + \frac{p_N - 2p_P + p_S}{\Delta y^2} \quad (14)$$

At the *bottom left corner* $\frac{\partial p}{\partial x_w} = \frac{\partial p}{\partial y_s} = 0$, which leads to $p_W = p_P$ and $p_S = p_P$. Thus:

$$\frac{\partial}{\partial x_j} \frac{\partial}{\partial x_j} p = \frac{p_E - p_P}{\Delta x^2} + \frac{p_N - p_P}{\Delta y^2} \quad (15)$$

The discrete Poisson equation can be solved on uniform and non-uniform Cartesian grids using pointwise Gauss-Seidel, pointwise-SOR or line-SOR linear solvers. Solutions to the Laplacian of cosines along x - and y - obtained on uniform and non-uniform grids are shown in Figure 2.

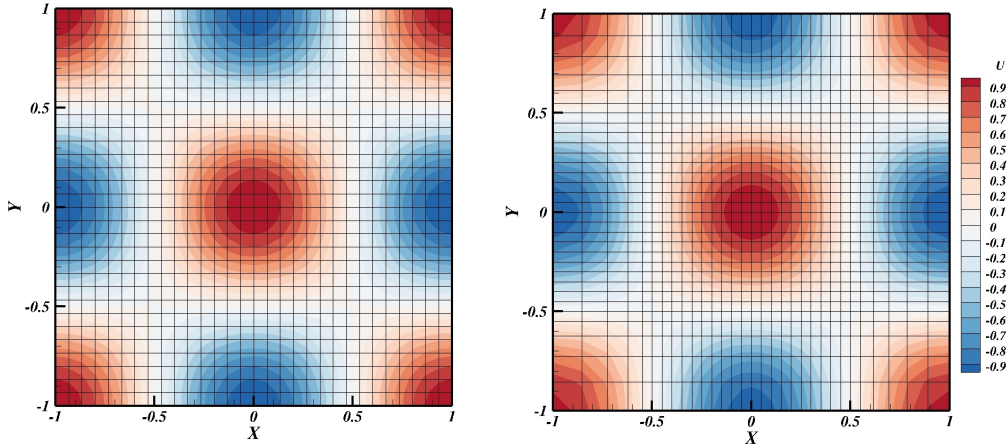


Figure 2: Solution to the two-dimensional Poisson equation, recovering cosines on (a) uniform and (b) non-uniform grids.

2.3. Navier-Stokes solver flowchart

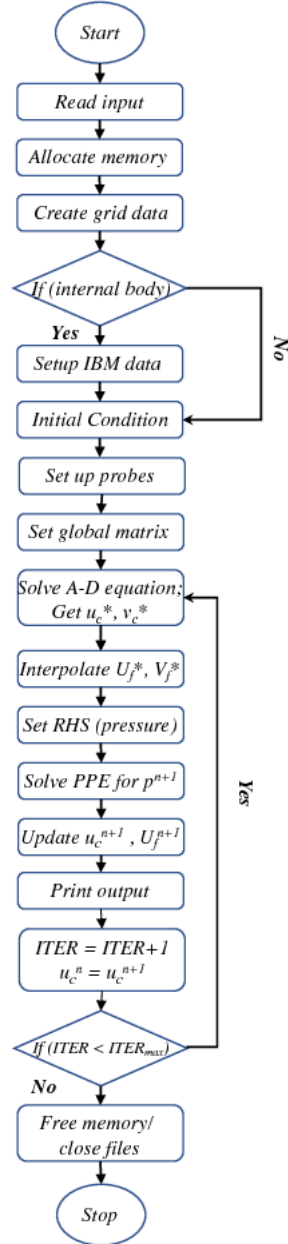


Figure 3: Flowchart for the NS-IBM solver

3. Results and Discussion

In this section, results are presented for various cases of channel flow, with and without immersed obstacles. For convenience, the channel is assumed to be symmetric about $y = 0$. In each case, the left boundary is the inlet, with flow confined between the top and bottom no-slip walls and leaving the channel through the right outlet boundary.

3.1. Free-Stream preservation

To test the correct implementation of the discretized Navier-Stokes equations, steady-state Poiseuille flow at Reynolds number 100 is simulated, in the absence of any internal bodies. The problem has the following analytic steady-state solution in which the viscous fluxes are balanced by the pressure gradient:

$$U(y) = 1 - 4y^2 \quad (16)$$

$$p(x) = p(0) - \frac{8x}{Re} \quad (17)$$

The Reynolds number is defined as $U_{max}H/\nu$, where H is the channel width, U_{max} the maximum velocity of the flow and ν the kinematic viscosity. An 80×40 rectangular grid (Figure 4) is used to discretize the domain and the steady-state analytic solution is used for the initial condition. By maintaining appropriate boundary conditions at the four edges of the domain, the initial condition is marched in time for 400 time-steps.

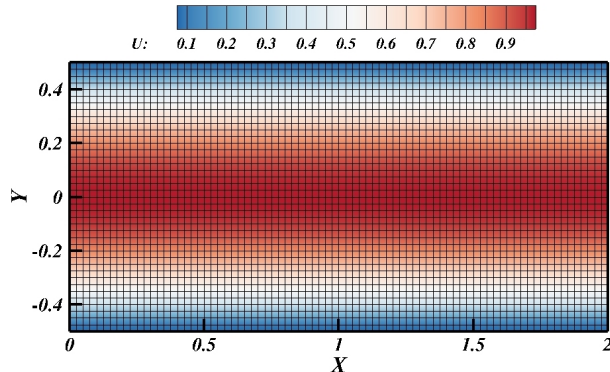


Figure 4: Grid configuration and steady-state streamwise velocity contour

The resulting streamwise velocity and pressure profiles are shown in Figure 5. Both profiles compare well with the analytic solutions.

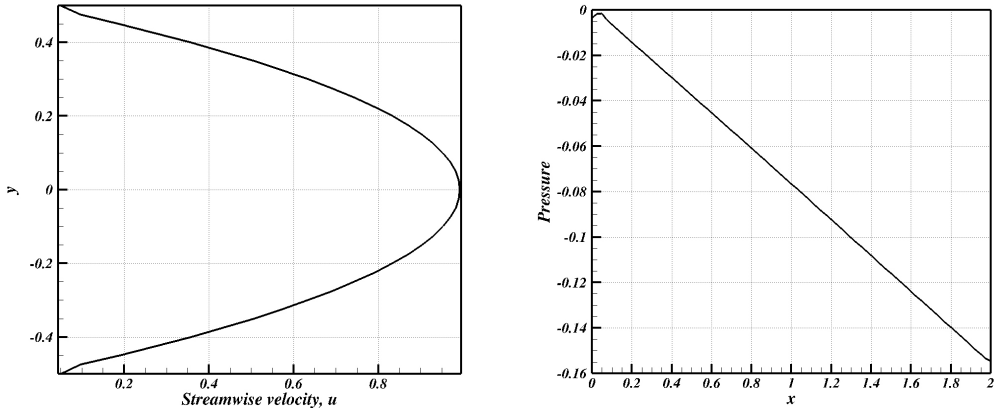


Figure 5: (a) Steady-state parabolic velocity profile variation along channel width and (b) pressure variation along channel length, indicating a linear pressure gradient.

3.2. Flow over square cylinder at $Re = 50$

In the next set of simulations, a square cylinder of edge length A is placed in the channel, centered around half-channel width and 4 edge lengths from the inlet boundary. The channel dimensions are: width $H = 8A$ and length $L = 16A$. The Reynolds number, defined as $U_{max}A/\nu$, was set to 50 and results were compared with those of (Breuer et al., 2000).

3.2.1. Steady-state velocity profile

At $Re < 60$, a steady wake develops behind the cylinder (Breuer et al. (2000)). Such a wake, along with flow streamlines, is shown in Figure 6. At finite Reynolds numbers < 60 , flow separates at the top and bottom edges of the cylinder, leading to a recirculation region attached to the trailing face of the cylinder. Within the recirculation region, two stationary and counter-rotating vortices, attached to each other, are observed. The streamlines also indicate that flow within the recirculation region does not leave the region. The thickness of the region decreases with distance from the trailing edge of the cylinder. Flow outside the region bends around it before eventually becoming parallel to the horizontal axis far away from the cylinder.

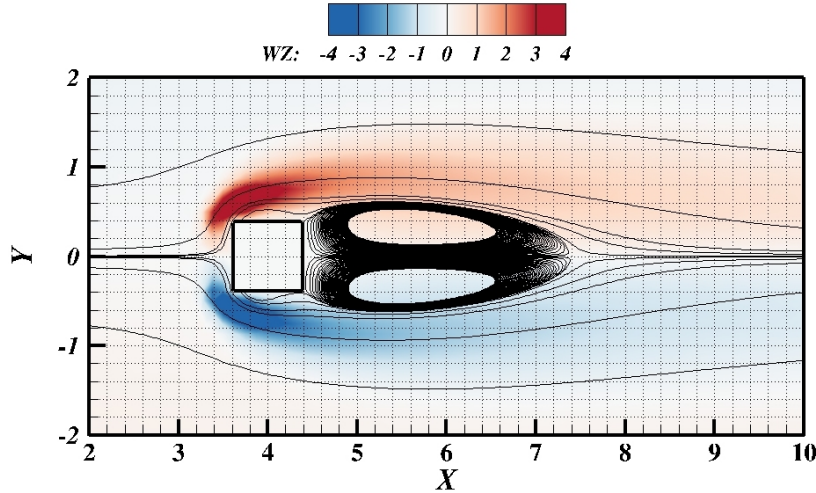


Figure 6: Steady-state streamlines and vorticity contours for flow over square cylinder at $Re = 50$, indicating the recirculation zone. The estimated length of this zone, relative to the dimension of the cylinder is 2.9.

Velocity profiles along channel length, at half-width, and along channel width, at $x = 5, 6, 10$, are shown in Figures 7(a) and 7(b), respectively. The streamwise velocity decreases rapidly from U_{max} at the inlet to zero at the cylinder leading edge, decreases to a negative minimum in the recirculation region and again increases to a positive value outside the recirculation zone, but does not recover the maximum amplitude of the parabolic profile. A stable discontinuity is observed at the inlet that develops due to the singularity in pressure at the corners of the inlet boundary. The discontinuity, however, does not grow into the bulk of the domain keeping the simulation stable.

The streamwise velocity at three sections downstream of the cylinder are shown in 7(b). Within the recirculation region ($x = 5, 6$), the velocity becomes negative, while the adjacent layers of fluid (increasing $|y|$) experience local acceleration leading to velocities larger than the amplitude of the incoming parabolic profile. This can also be explained as a consequence of mass-balance immediately upstream and downstream of the cylinder. Due to blockage in the channel, the flow upstream of the cylinder must squeeze through a smaller area while maintaining a constant mass flow rate. This leads to regions in the fluid with velocities larger than the maximum inlet velocity.

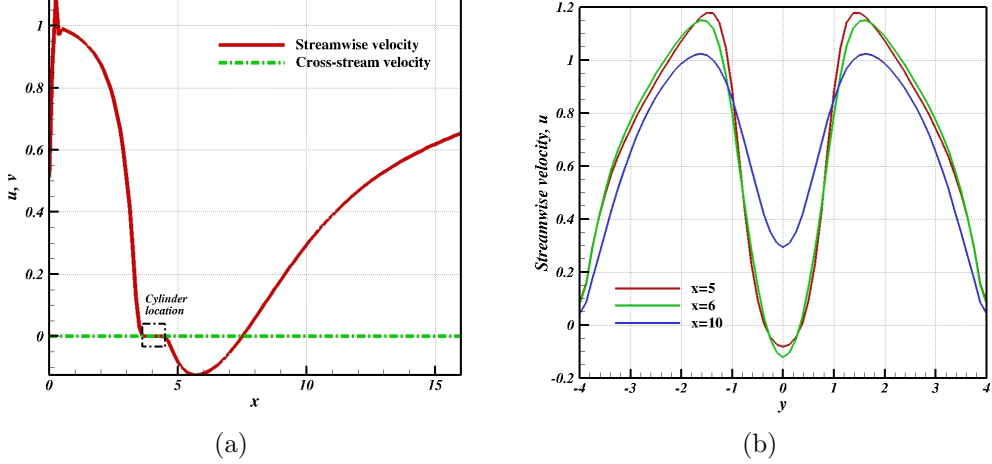


Figure 7: (a) Steady-state velocity profile at half-channel width and (b) steady-state streamwise velocity profile at $x = 5, 6, 10$

3.2.2. Recirculation Length

The length of this recirculation region, along the centerline grows linearly with Reynolds number and is given by equation 18 (Breuer et al. (2000)):

$$\frac{L_r(Re)}{A} = -0.065 + 0.0554Re \quad (18)$$

The recirculation length in the simulation can be computed from the steady-state streamline plot by measuring the distance between trailing edge of the cylinder and the end of the recirculation region along the line of symmetry. This information can also be extracted from Figure 7(a), as the distance between the two points downstream of the cylinder where the streamwise velocity crosses the zero mark. The recirculation length is estimated to be 2.9. A comparison with the variation in L_r with Re obtained from the analytic formula is shown in Figure 8. The analytic value for the recirculation length is 2.705. The computed value has, therefore, about 7% error.

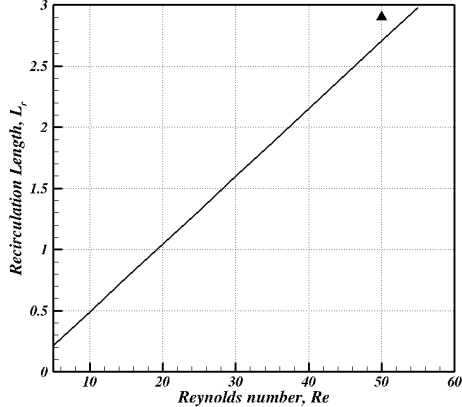


Figure 8: Comparison of computed recirculation length (Δ) with that obtained from the analytic formula provided by Breuer et al. (2000)

3.3. Flow over cylinder at $Re = 150$

Next, keeping the grid and domain parameters constant, the Reynolds number of the flow is increased to 150. A time-step was chosen such that moderate CFL ($\approx 0.6 - 0.7$) were maintained. The flow regime should no longer result in a steady wake behind the cylinder. Four snapshots of vorticity contours with corresponding streamlines for this test case are illustrated in Figure 9. A wake starts developing behind the cylinder and remains attached for some time as it continues to grow (9(a)). After some time, the wake becomes unstable and round-off errors in calculations are sufficient to trip it such that it starts separating from the cylinder trailing edge (Figure 7(b)). This is the onset of vortex shedding from the cylinder. The wake behind the cylinder transitions to an unstable mode where it alternately sheds periodic, counter-rotating vortices (Figures 9(c), 9(d)), resulting in a Kármán vortex street downstream of the cylinder.

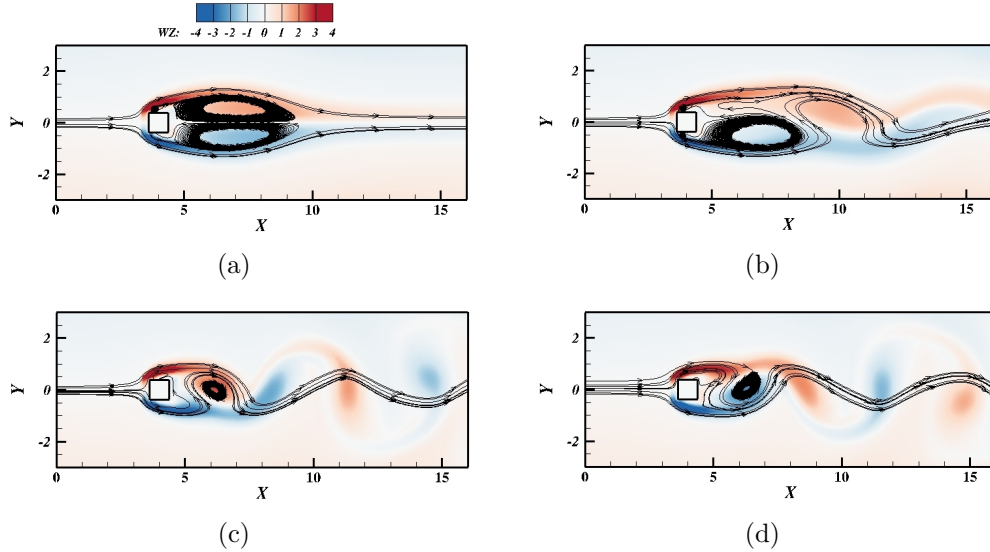


Figure 9: Snapshots of vorticity contour plots and streamlines for flow past the square cylinder (Baseline case) at $Re = 150$ at four time instants indicating (a) Development of recirculation zone in the cylinder wake, (b) onset of vortex shedding, (c-d) Kármán vortex street in the wake of the cylinder.

Figures 10(a) and 10(b) show the variation of the streamwise and cross-stream velocity components, respectively, along the length of the channel, at channel half-width. They provide a qualitative comparison to results of (Breuer et al., 2000). The streamwise velocity profile looks similar to the test case for $Re = 50$, upstream of the cylinder. However, past the cylinder, the velocity rises to nearly the amplitude of the inlet velocity. Due to the presence of a vortex street, the velocity plots have bumps which give a rough estimate of the number of vortices in the wake of the cylinder.

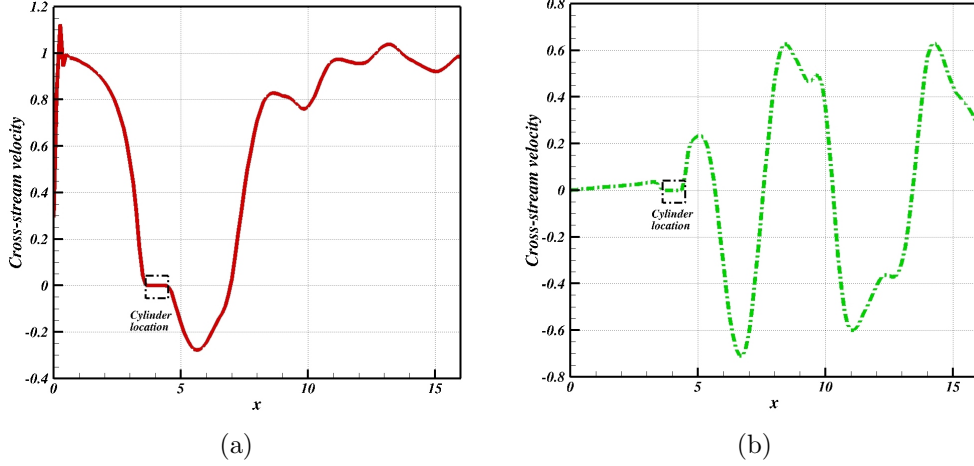


Figure 10: Variation of (a) streamwise and (b) cross-stream velocity components along length of the channel at half-width, indicating the location of cylinder.

The Strouhal number is a non-dimensional number that gives a measure of the vortex shedding frequency for the system. It is defined as $St = fA/U_{max}$, where f is the vortex shedding frequency, which is computed from the vertical velocity component at a probe located $2A$ units behind the cylinder. Figure 11 shows the evolution of vertical velocity recorded by the probe and results of the DFT analysis on this signal. The Strouhal number was computed through spectral analysis to be 0.135.

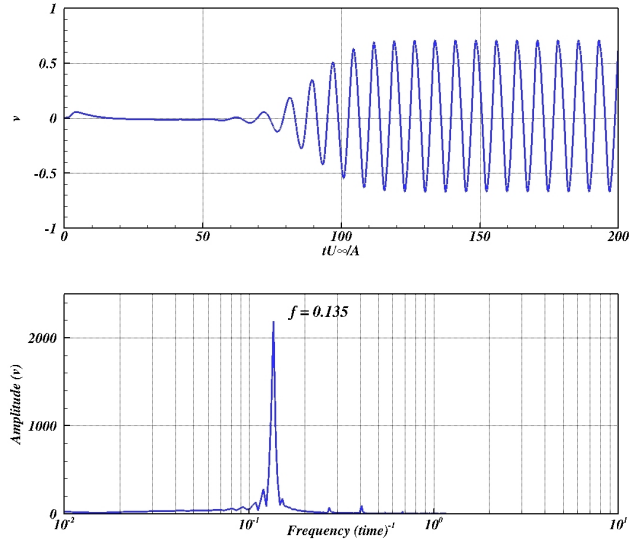


Figure 11: (top) Evolution of vertical velocity component at a distance $2A$ downstream of the cylinder and (bottom) energy content of the spectrum of the detected frequencies from DFT analysis of the probe signal.

3.4. Grid dependence test

In this section, the influence of grid refinement on solution accuracy is studied. The same domain as in section 3.3 was discretized using twice as many points (265×128) along $x-$ and $y-$, respectively. Again, time-step was chosen such that $CFL \approx 0.6 - 0.7$ at all times. The flow characteristics, probe velocity and resulting Strouhal number were computed. Figure 12 shows vorticity contours and streamlines at four time-instants as was done in the previous section.

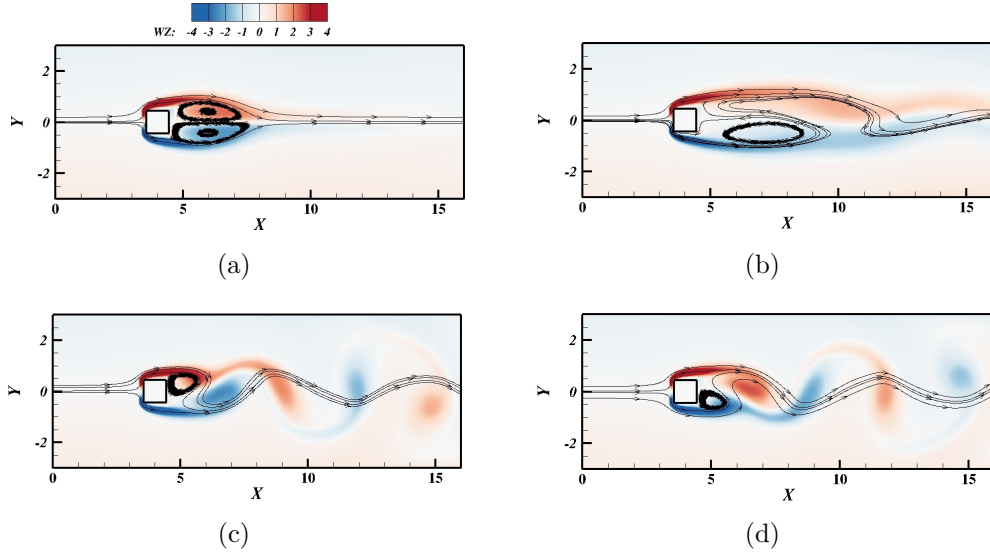


Figure 12: Snapshots of vorticity contour plots and streamlines for flow past the square cylinder (grid dependence case) at $Re = 150$, on a 256×128 grid, at four time instants indicating (a) growth of wake, attached to the cylinder, (b) onset of vortex shedding, (c-d) Kármán vortex street in the wake of the cylinder.

Figure 13 shows the vertical velocity at the probe and the Strouhal frequency, obtained through spectral analysis, as 0.145. This value is different from the one reported in section 3.3, albeit of the same order, indicating a possible improvement in result owing to a smaller truncation error.

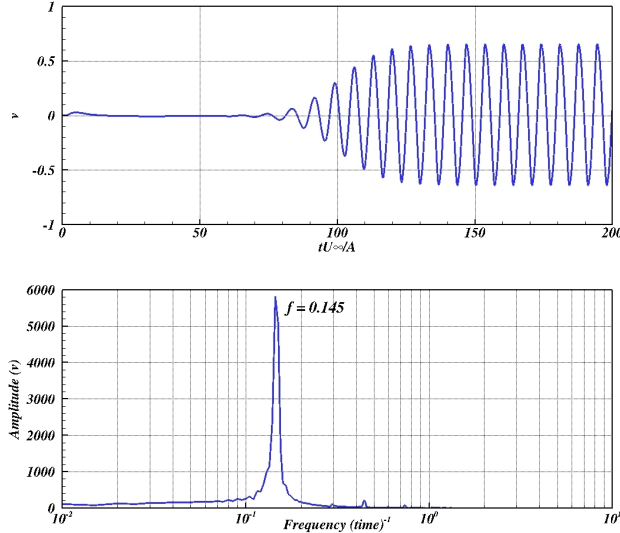


Figure 13: (top) Evolution of vertical velocity at the probe location and (bottom) energy of the frequency spectrum for the probe signal, showing the most energetic frequency = 0.145.

3.5. Domain Dependence tests

The objective of this section is to demonstrate that the solver can produce similar results, irrespective of domain parameters as long as they do not define some characteristic length. In this case, the domain length and cylinder location are varied and results compared with those from section 3.3.

3.5.1. $L/A = 24$; $d/A = 4$

First, a larger domain with length $L = 24A$ is used and the cylinder is placed at a distance $4A$ from the inlet, centered along channel half-width. The same analysis as in the previous sections is performed. Figure 14 illustrates vorticity contours and streamlines around the cylinder at different time-intervals, indicating different stages of the vortex-shedding phenomenon.

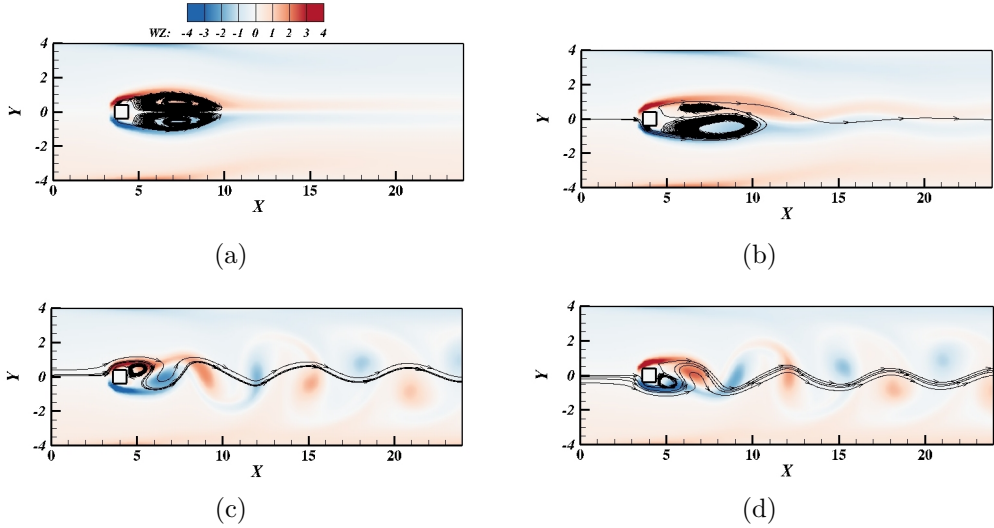


Figure 14: Snapshots of vorticity contour plots and streamlines for flow past the square cylinder at $Re = 150$ (Domain dependence case 1) at four time instants indicating (a) Development of recirculation zone in the cylinder wake, (b) onset of vortex shedding, (c-d) Kármán vortex street in the wake of the cylinder.

The Strouhal number for this case (Figure 15) was obtained as 0.137, which is close to the one reported in section 3.3.

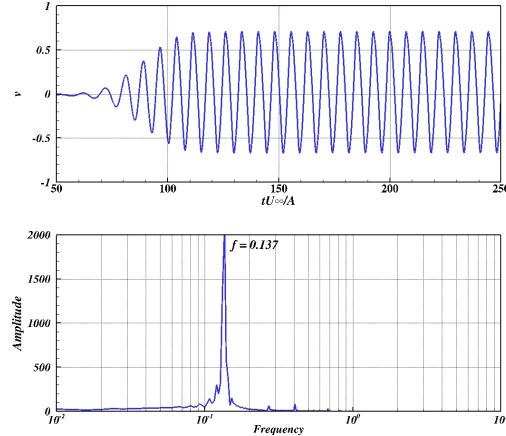


Figure 15: (top) Time-varying probe velocity and (bottom) results of spectral analysis to find the vortex shedding frequency.

3.5.2. $L/A = 24$; $d/A = 8$

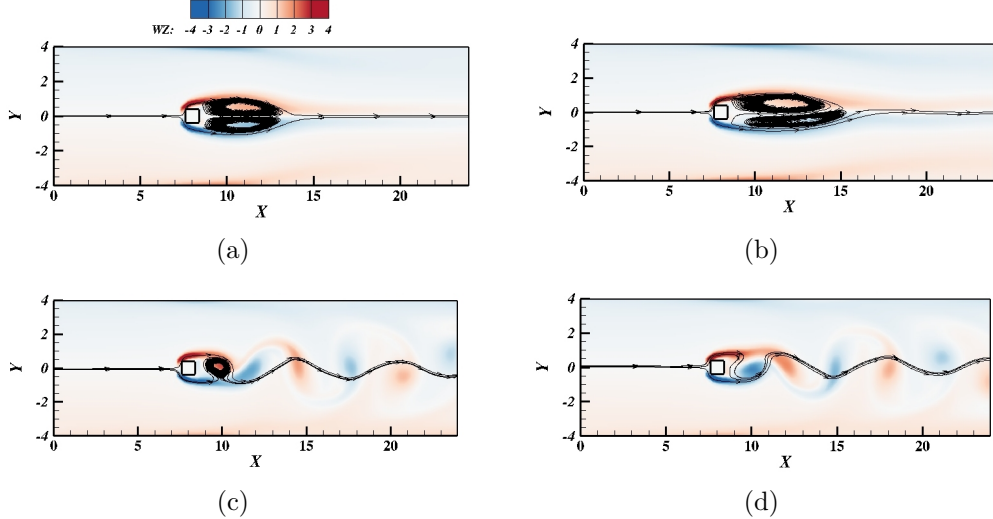


Figure 16: Snapshots of vorticity contour plots and streamlines for flow past the square cylinder at $Re = 150$ (Domain dependence case 2) at four time instants indicating (a) Development of recirculation zone in the cylinder wake, (b) onset of vortex shedding, (c-d) Kármán vortex street in the wake of the cylinder.

Next, the cylinder is moved away from the inlet, such that $d/A = 8$ and the resulting flow fields and vorticity contours are shown in Figure 16, while the computed vortex-shedding frequency is shown in Figure 17. Again, the computed Strouhal number, 0.136, is very close to the one reported in section 3.3. *The results in this section together with those from sections 3.3, 3.5.1 demonstrate that the solution is independent of the domain.*

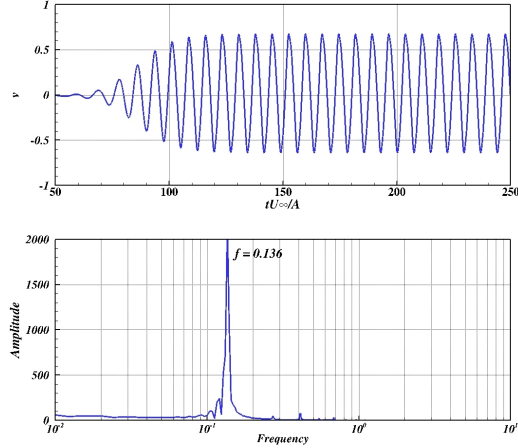


Figure 17: (top) Time-varying probe velocity and (bottom) results of spectral analysis to find the vortex shedding frequency.

3.6. Comparison of Strouhal number with (Breuer et al., 2000)

Figure 18(b) shows a comparison between the variation of vertical velocities recorded by the probe with time, in the simulations described in sections 3.3 - 3.5. The waveforms for the Baseline and two domain dependence cases ($d/A = 4$ and $d/A = 8$) appear to have the same or very similar frequencies of oscillation, although they are separated through some phase difference. On the other hand the waveform from the grid refinement study ($2 \times$ refinement) seems to oscillate at a different frequency as compared to the first three waveforms. This is further corroborated by the fact that only this case resulted in a Strouhal (vortex shedding) frequency different from the one from the baseline case.

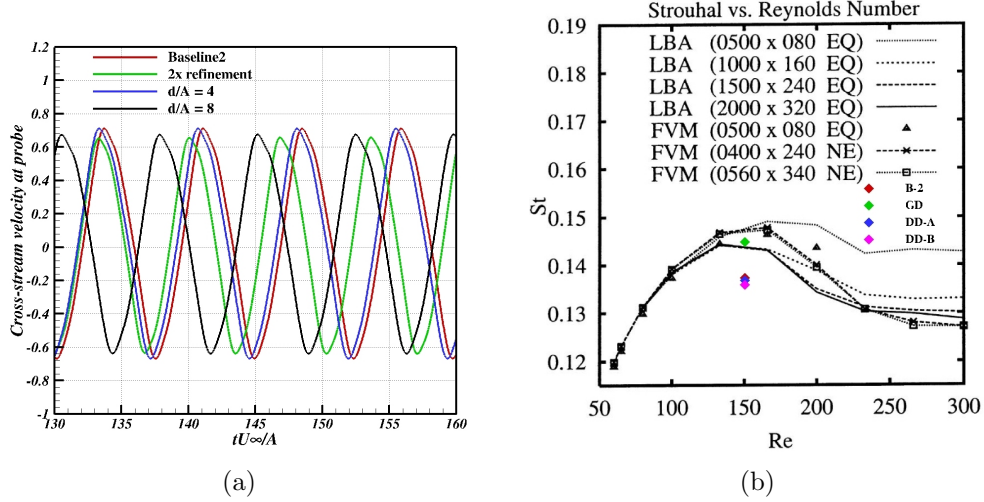


Figure 18: (a)Comparison between the evolution of vertical velocity at the probe in wake of the cylinder for the baseline 2, grid dependence and the two domain dependence tests. In each case, the probe was situated $2A$ units behind the trailing edge of the cylinder. (b) Shows draws a comparison between the computed Strouhal numbers in each case with the Re-St variation presented by (Breuer et al., 2000). Note that the test cases are abbreviated as: Baseline 2 (B-2), Grid dependence test (GD), Domain dependence test 1 (DD-A) and Domain dependence test 2 (DD-B).

A comparison between the computed Strouhal numbers and the published results Breuer et al. (2000) is shown in Figure 18(a). While St obtained in sections 3.3 and 3.5 all show nearly the same error from published results ($\approx 7\%$), the result obtained from using a doubly refined grid (section 3.4) is in very good agreement with published trends for St . *This implies that the numerical solution is independent of the domain used, but is more accurate with increasing grid resolution.*

3.7. Flow past circular cylinder at $Re = 100$

To test the versatility of the implemented immersed boundary method, a non-conforming solid boundary needs to be tested for solution accuracy. Therefore, in the following test case, the flow past a circular cylinder of diameter $D = 1$, confined in a rectangular channel, is simulated. The Reynolds number for this problem is 100 and 20% blockage ($H/D = 5$) is chosen. The length of the channel is $16D$. In order to sufficiently resolve the curvature of the circular cylinder, a uniform grid resolution of 0.0625 (256 × 80 grid) is used along both directions. The domain, relative to the cylinder, the grid and the boundary conditions are shown in Figure 19. Results obtained in this study are compared against those of Griffith et al. (2011).

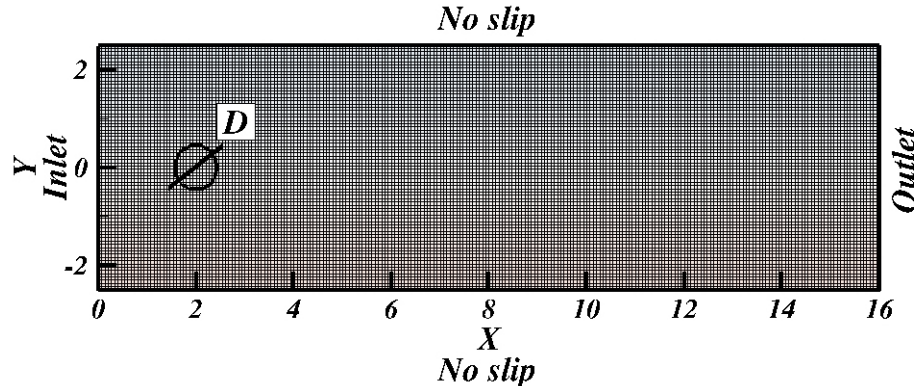


Figure 19: Schematic representation of the test case, indicating the domain and cylinder dimensions, grid size and boundary conditions.

Snapshots of vorticity contours along with streamlines in the vicinity of the cylinder, at different time intervals, is shown in Figure 20. As was seen in the several cases with the square cylinder, the flow over a circular cylinder follows similar mechanisms in that it first develops a growing wake, attached to the cylinder. Beyond a point, the wake becomes unstable and can be tripped into separation, after which, alternating counter-rotating vortices, forming a Kármán vortex street downstream, are shed from the cylinder.

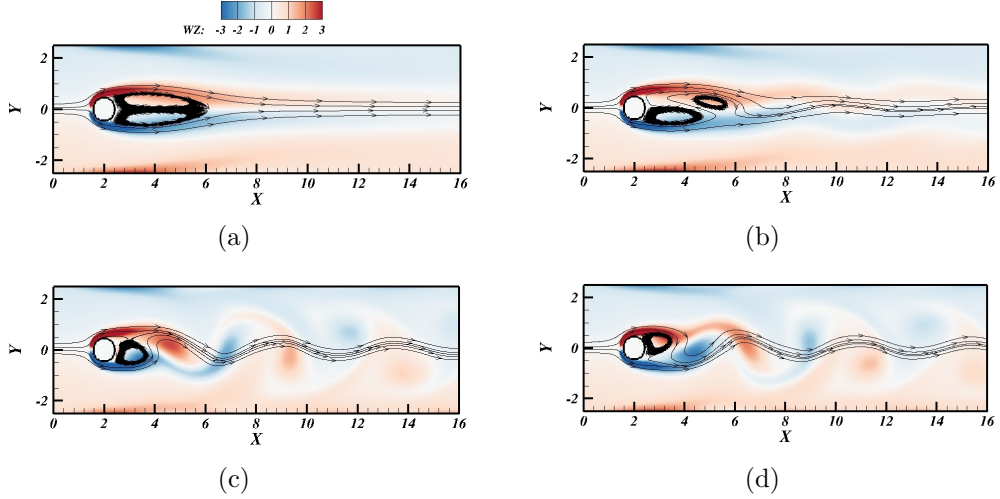


Figure 20: Snapshots of vorticity contour plots and streamlines for flow past the circular cylinder at $Re = 100$ at four time instants indicating (a) Development of recirculation zone in the cylinder wake, (b) onset of vortex shedding, (c-d) Kármán vortex street in the wake of the cylinder.

The same analysis was performed in this test case, wherein a probe was placed at a distance $2D$ behind the cylinder and the evolution of the vertical velocity is tracked. The Kármán vortex street results in an oscillating vertical velocity (Figure 21(a) – top) at the probe and the most energetic frequency of oscillation represents the fundamental vortex shedding frequency. This Strouhal frequency is identified through Fourier analysis of the oscillating signal and is computed to 0.178 (Figure 21(a) – bottom).

A comparison between the Strouhal number from the present analysis with published results (Griffith et al. (2011)), is illustrated in Figure 21(b). Griffith et al. (2011) computed St as a function of Re , for several blockage ratios. Present results are in excellent agreement with their St –trend for 20% channel blockage.

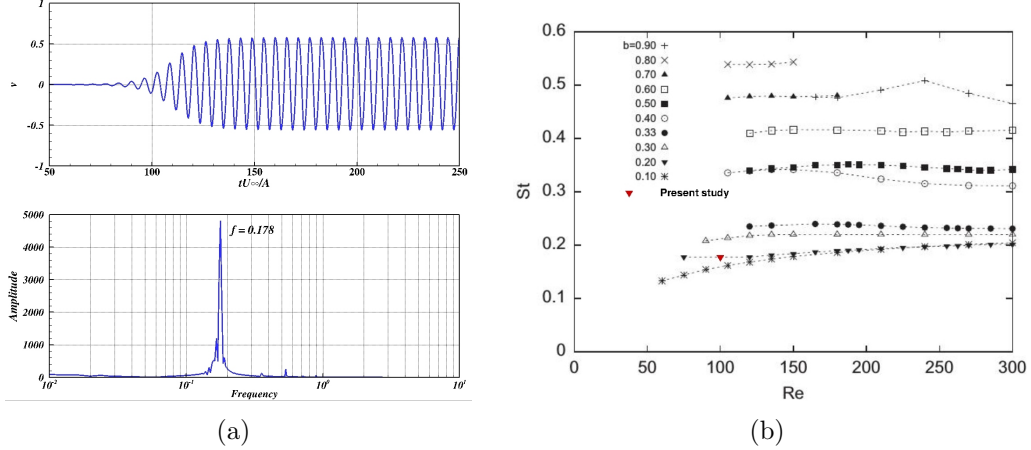


Figure 21: (a) (top) Evolution of vertical velocity component at a distance $2A$ downstream of the cylinder and (bottom) results for the spectral analysis of the $-v$ signal in time, indicating the Strouhal frequency, computed to 0.178. (b) shows a comparison of computed Strouhal number (St), plotted as a function of Reynolds number (Re) with published data of Griffith et al. (2011). The computed (Re, St) coordinate (red inverted triangle) is overlaid on the line plots of Griffith et al. (2011) for effective visualization.

4. Conclusion

Thus, in this report, the development of a two-dimensional Navier-Stokes solver is described. Second-order central differencing scheme was used to compute discrete derivatives. The coupled fluid system was marched in time using Chorin's fractional step method. The advective and diffusive fluxes were integrated in time using second-order explicit Adams-Bashforth and implicit Crank-Nicolson integration schemes, respectively. Point-wise Gauss-Seidel and SOR based linear solvers were used to invert the implicit momentum equation advance and the pressure Poisson system, respectively. By incorporating a first-order immersed boundary method, flow around rigid bodies was modeled. The ability of the solver of maintaining uniform channel flow, in the absence of immersed bodies was demonstrated. Then, the flow around a square cylinder in a rectangular channel was simulated at Re 50 and 150. The recirculation length for Re 50 and the Strouhal number of the vortex shedding frequency at Re 150 were measured and compared against results of Breuer et al. (2000). The Strouhal number was computed from spectral analysis of the vertical component of velocity at a point downstream of the cylinder. Further, these results were shown to be independent of the domain used in the simulation, as long as characteristic dimensions were unchanged. A grid dependency test also showed some improvement in results, showing some error scaling with grid size. Finally, the flow over a circular cylinder, confined in a channel with 20% blockage, was simulated at Re 100. The numerical results, thus obtained, were in excellent agreement with those of Griffith et al. (2011). Thus, the Navier-Stokes solver developed herein was validated for several problems demonstrating its versatility.

References

- M. Breuer, J. Bernsdorf, T. Zeiser, and F. Durst. Accurate computations of the laminar flow past a square cylinder based on two different methods: lattice-boltzmann and finite-volume. *International Journal of Heat and Fluid Flow*, 21(2):186–196, 2000.
- Martin D. Griffith, Justin Leontini, Mark C. Thompson, and Kerry Hourigan. Vortex shedding and three-dimensional behaviour of flow past a cylinder confined in a channel. *Journal of Fluids and Structures*, 27(56):855 – 860, 2011.